Disguised Tailing and Video Surveillance With Solar-Powered Fixed-Wing Unmanned Aerial Vehicle

Shuyan Hu, *Member, IEEE*, Wei Ni, *Senior Member, IEEE*, Xin Wang, *Senior Member, IEEE*, and Abbas Jamalipour, *Fellow, IEEE*

***Abstract*—Disguised tailing and visual monitoring of suspicious mobile targets is a promising application of security unmanned aerial vehicles (UAVs). But trajectory planning is non-trivial, especially for fixed-wing UAVs with more constrained maneuverability and dynamic models. This paper proposes a new framework to optimize collectively the propulsion power and the three-dimensional (3D) trajectory of a solar-powered, fixed-wing UAV on a disguised tailing and video surveillance mission. The multi-objective optimization strikes a balance between distance keeping, elevation variance, and power efficiency. A key aspect is that we develop a new propulsion power model of the fixed-wing UAV by analyzing the forces undergone while the UAV is ascending or descending. Another important aspect is a series of non-trivial reformulations, which convexify the multi-objective problem progressively with increasingly tightening linear approximation and solve the problem with a polynomial time-complexity. Our algorithm can control the trajectory of the UAV on-the-fly. Simulations confirm that the algorithm outperforms existing schemes in terms of visual disguise and power efficiency. The fixed-wing UAV also demonstrates its advantage of energy efficiency and sustainability to elongate the surveillance mission, over its rotary-wing counterpart.**

***Index Terms*—Disguised visual monitoring, fixed-wing UAV, solar power harvesting, trajectory design, successive convex approximation, model predictive control.**

I. Introduction

With fast maturing automation and onboard processor technologies, unmanned aerial vehicles (UAVs) are increasingly deployed for search and rescue [1], bushfire monitoring [2], relaying [3], [4], and surveillance [5], [6]. Equipped with sensors and cameras, UAVs are also employed to tail mobile targets [7] and detect street crimes [8]. Fixed-wing UAVs of various sizes are known for fast speed, energy efficiency, and quietness. They can be particularly suitable for tracking and surveillance missions [9]. On the other hand, adversarial targets may detect the monitor, execute countermeasures, and put public safety at stake. It could be crucial for UAV monitors, in particular, fixed-wing UAV monitors, to disguise themselves and bewilder the targets in their missions.

Little to no existing studies have investigated the disguise of the UAV monitor during the tailing or surveillance mission. Most existing designs have required a UAV monitor to keep the target within its view for video surveillance and image-aided tracking. Image-aided control approaches have been proposed for a UAV monitor to tail a mobile target [10]–[13], calculate the three-dimensional (3D) geological position of a mobile target [14], or detect a hidden stationary target [15]. In [10], geometric control was performed with nonlinear multi-ranking control, without requirement of a calculable thrust force. In contrast to traditional backstepping approaches, the geometric control could potentially simplify the execution of steps. Relying on the Lyapunov theory, the image-aided method was shown to converge. UAV-based target tailing was pursued in [16] and [17] to address visual obstruction in a city with high-rises. The route of a UAV monitor was designed to achieve the maximum detection rate, which is captured by the probability of keeping the target within its view. A time-varying zero-sum matching was developed in [18] to find the best moving direction for the monitor, who attempts to have the target in vicinity and sight. Dynamic programming was employed to achieve the lowest sum price pertaining to the target-monitor spatial separation. Of all the existing works on UAV-enabled target tailing, e.g., [10]–[17], the design of 3D UAV route was only addressed in [12]. The rest supposed that the monitoring UAV traveled at a fixed altitude and designed 2D routes to require the UAV to fly horizontally. A multi-objective optimization problem was formulated in [12] in pursuit of the least power consumption of a UAV monitor, and the largest number of visible targets. None of the above works have taken disguise into their designs.

Limited power supply to a UAV monitor could restrain tailing and monitoring missions. Most existing UAVs are powered by batteries, limiting the mission time and distance. The trajectory of a UAV monitor should be meticulously designed to elongate the mission, as mentioned in [11]–[13]. Realistic power usage models characterizing various flight statuses, including

Manuscript received May 25, 2021; revised December 19, 2021; accepted March 6, 2022. Date of publication March 8, 2022; date of current version May 20, 2022. This work was supported in part by the National Natural Science Foundation of China under Grants 62071126 and 62101135, in part by the Innovation Program of Shanghai Municipal Science and Technology Commission under Grants 20JC1416400 and 21XD1400300, and in part by the China Postdoctoral Science Foundation under Grant 2020M681168. The review of this article was coordinated by Dr. Joongheon Kim. *(Corresponding author: Xin Wang.)*

Shuyan Hu is with the Key Lab of EMW Information (MoE), the School of Information Science and Technology, Fudan University, Shanghai, Yangpu District 200433, China (e-mail: syhu14@fudan.edu.cn).

Wei Ni is with the Data61, Commonwealth Scientific and Industrial Research Organization, Sydney, NSW 2122, Australia (e-mail: Wei.Ni@data61.csiro.au).

Xin Wang is with the Key Lab of EMW Information (MoE), the Department of Communication Science and Engineering, Fudan University, Shanghai, Yangpu District 200433, China (e-mail: xwang11@fudan.edu.cn).

Abbas Jamalipour is with the School of Electrical and Information Engineering, The University of Sydney, Sydney, NSW 2006, Australia (e-mail: a.jamalipour@ieee.org).

Digital Object Identifier 10.1109/TVT.2022.3157705

propulsion, thrust and hanging, should be considered. Yet, the energy usage of the UAV monitor was simplified to a linear function of its velocity in [11] and [12], whereas the power usage of the hovering state was not considered in [13]. On the other hand, ambient energy harvesting, solar power in particular, has been increasingly utilized in fixed-wing UAV platforms, e.g., [19]. Many latest fixed-wing UAVs can carry a payload of as much as 10 kg. It is plausible for such UAVs to be equipped with solar panels, e.g., on the top of the UAVs. For example, SolarXOne by a French company XSun is a fully electric, solar-powered autonomous drone [20]. Sunbird SB4 Phoenix is another commercially available solar-powered drone [21]. The harvested solar power can potentially energize the UAVs' tracking and surveillance missions for sustainability and longevity.

This paper presents a new approach to the trajectory plan of a solar-powered, fixed-wing UAV on a disguised, UAV-on-UAV surveillance mission, in which the monitoring UAV (or "monitor") tails and visually monitors a suspicious UAV (or "target"). The monitor camouflages its surveillance attempt and confuses the target by adaptively changing its heading and elevation. By this means, the monitor appears far away and flies in seemingly irrelevant directions, keeping the target unwary. The monitor adjusts its trajectory and direction adapting to the solar energy reaping amount, hence elongating the mission duration and sustainability.

The key contributions of our work are summarized as follows.

- A new algorithm is developed to allow a solar-powered, fixed-wing UAV to carry out a disguised tailing and video surveillance mission, where the trajectory of the UAV is optimized to strike a balance between the multiple objectives of distance keeping, elevation variance, and power efficiency.
- The algorithm is based on a new propulsion power model of the fixed-wing UAV under a 3D trajectory, developed by meticulously analyzing the forces undergone while the UAV is ascending or descending.
- The algorithm involves a series of non-trivial reformulations, which convexify the multi-objective problem (including the constraints on the maneuverability of the UAV) progressively with increasingly tightening linear approximation and solve the problem in polynomial time.
- In coupling with receding horizon control, the proposed algorithm is applied online to deliver adaptive control of the UAV and refine the trajectory on-the-fly.

Extensive simulations confirm that the proposed scheme outperforms alternative schemes with no or partial disguise, in terms of visual disguise and power efficiency. As compared with a rotary-wing UAV, the fixed-wing UAV shows its advantage of energy efficiency and sustainability to elongate the surveillance mission. Such UAV-enabled visual monitoring can find critical implementations to domestic and civil security.

To the best of our knowledge, there has been no existing study on the trajectory design of a solar-powered, fixed-wing UAV for a disguised video tracking and surveillance mission. In our recent work [22], the trajectory of a solar-powered, rotary-wing UAV was optimized for a stealthy video tracking and surveillance task. Compared to [22], the novelty of this paper is three-fold: (i) a new 3D propulsion power model is developed to capture the ascent and descent of fixed-wing UAVs, which has never been captured in the existing literature; (ii) a fixed-wing UAV is considered in this paper, which necessitates a new solution different from the one developed in [22] due to the distinctive and more constrained maneuverability and dynamic model as well as the distinctive propulsion power model of fixed-wing UAVs; and (iii) different from the offline algorithm developed in [22], the proposed solution in this paper is online and can refine the UAV trajectory on-the-fly by incorporating the receding horizon control and the successive convex approximation.

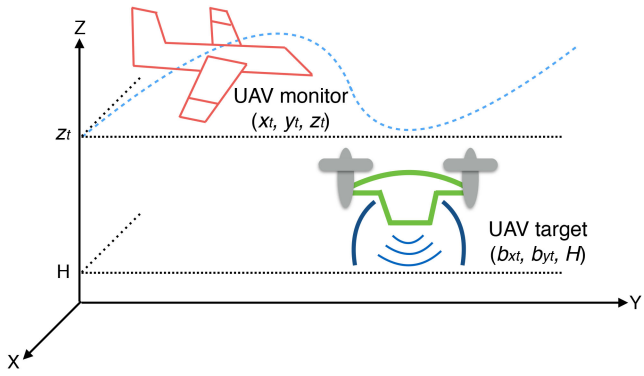

Fig. 1. A solar-powered, fixed-wing monitoring UAV carries out disguised tailing and video surveillance on a targeted rotary-wing UAV, where the monitoring UAV plans its trajectory adapting to the movement of the targeted UAV. The monitoring UAV also keeps its distance to the target, and keeps varying its elevation to bewilder the latter.

The remainder of this paper is arranged as follows. Section II provides the model of the considered system. Section III derives the 3D propulsion power of a fixed-wing UAV, and formulates the problem of disguised tailing and video surveillance by the UAV. Section IV articulates our online method for tackling the problem of joint power and trajectory optimization. The proposed method is numerically evaluated in Section V, followed by concluding remarks in Section VI.

II. System Model

Consider a solar-powered, fixed-wing UAV on a disguised tailing and video surveillance mission, where a target UAV flies at the altitude of H (in meters), as illustrated in Fig. 1. The mission lasts T seconds, which is evenly split into N time slots with a duration of δ seconds per slot ($T = \delta N$).

A. UAV Mobility

Let $\boldsymbol{b}_t := (b_{xt}, b_{yt}, H)$ and $\boldsymbol{q}_t := (x_t, y_t, z_t)$ collect the 3D waypoints of the target and the monitor at time slot t, respectively, $t = 1, \ldots, N$. Let $\boldsymbol{v}_t := (v_{xt}, v_{yt}, v_{zt})$ and $\boldsymbol{a}_t := (a_{xt}, a_{yt}, a_{zt})$ collect the velocity and acceleration of the UAV monitor in the 3D space at time slot t, respectively.

The fixed-wing UAV monitor needs to obey the following mobility constraints [9]:

$$\boldsymbol{q}_{t+1} = \boldsymbol{q}_t + \boldsymbol{v}_t\delta + \frac{1}{2}\boldsymbol{a}_t\delta^2, \forall t, \tag{1a}$$

$$\boldsymbol{v}_{t+1} = \boldsymbol{v}_t + \boldsymbol{a}_t\delta, \forall t, \tag{1b}$$

$$\|\boldsymbol{a}_t\| \leq a_{\max}, \forall t, \tag{1c}$$

$$\|\boldsymbol{v}_t\| \le v_{\max}, \forall t, \tag{1d}$$

$$v_{\min} \le \|\boldsymbol{v}_t\|, \forall t, \tag{1e}$$

$$v_{zt}/\|\boldsymbol{v}_t\| \le \vartheta, \forall t, \tag{1f}$$

where $a_{\max}$ denotes the maximum acceleration of the UAV monitor; $v_{\min}$ and $v_{\max}$ are the lower and upper bounds of the UAV speed, respectively; and ϑ is the sine of the maximum pitch angle of the UAV monitor. The current location of the monitor depends on its previous location, current velocity and acceleration, as captured in constraint (1a). The current velocity of the UAV monitor relies on its previous velocity and current acceleration, as captured in constraint (1b). Constraint (1f) makes sure that the UAV monitor ascends by a limited pitch angle. Constraints (1c)–(1e) are self-explanatory.

B. Visual Disguise

The time-dependent 3D distance, i.e., spatial separation, between the UAV monitor and the target is

$$d_t = \|\boldsymbol{q}_t - \boldsymbol{b}_t\|, \forall t. \tag{2}$$

By imposing $d_t \le d_{\max}$, the monitor can keep the target in sight and achieve meaningful visual resolution on the target. $d_{\max}$ (in meters) is the maximum allowed spatial separation.

Suppose that the UAV monitor is always traveling at a higher altitude than the target, i.e., $z_t \ge z_l > H, \forall t$, in which z_l is the lowest allowed elevation of the monitoring UAV. This assumption stems from the fact the 360° full-view surveillance camera is usually placed to the underbody of the UAV monitor. In light of [22], we consider that the monitoring UAV camouflages by maintaining a reasonable distance from the target, and continuously varying the elevation to bewilder the target. The continuously varying elevation of the monitor holds back the target from setting the correct focal length of its camera to the monitor, resulting in a blurry sight. Keeping a reasonable monitor-target distance hinders the target from getting satisfying visual resolutions on the monitor, even though its camera could be reasonably concentrated. The *disguise* of the monitor is characterized by its horizontal distance to the target and its continuously varying elevation:

$$f_t = \mu_1[(x_t - b_{xt})^2 + (y_t - b_{yt})^2] + \mu_2(z_t - z_{t-1})^2, \forall t \tag{3}$$

where μ_1 and μ_2 are two weighting coefficients to adjust the weights of the two aspects, respectively. The motivation of separating the disguising performance between the horizontal and vertical movement in (3) stems from the fact that the level flight and the ascending (or descending) of a fixed-wing UAV are typically controlled separately by controlling its rudder and elevator, respectively. Clearly, f_t is a convex function of (x_t, y_t, z_t, z_{t-1}) for any time slot t.

We further impose a constraint on the minimum target-monitor distance, as given by

$$d_{\min} \le d_t, \forall t, \tag{4}$$

where $d_{\min}$ specifies the minimum distance to be kept from the target to help the monitor with its disguise.

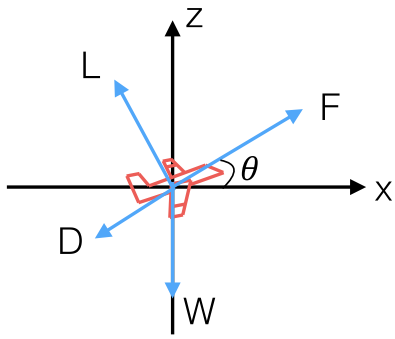

Fig. 2. An illustration of the forces on an ascending aircraft, where W, D, L and F stand for weight, drag, lift and thrust, respectively.

III. UAV Propulsion Power With 3D Trajectory and Problem Statement

A. Harvested Solar Power

Let P_s^t (in Watts) denote the solar power harvesting capability of the UAV monitor at any slot t. We suppose that the tailing task occurs at noon a sunny day. Per slot t, the harvested solar power is given by [23]

$$P_s^t(z_t) = \eta S P_i \exp\left(-\alpha\left(1 - 2.2556 \times 10^{-5} z_t\right)^{5.2561}\right), \tag{5}$$

where $\eta \in (0, 1)$ stands for the power-conversion efficiency, S (in m^2) is the size of the solar panel of the UAV monitor, P_i (in Watts) measures the fixed radiation intensity of solar beams before traveling through clouds, and $\alpha > 0$ is the total atmospheric extinction. The initial battery level of the UAV monitor is E_0 (in Joules) before the mission.

B. Propulsion Power

We first derive the propulsion power of the fixed-wing UAV with a 3D trajectory. As illustrated in Fig. 2, the fixed-wing UAV aloft undergoes four forces in total, namely, weight, drag, lift, and thrust at any instance [24].

- *Weight (W):* This is the force incurred by gravity with $W = mg$, in which m represents the UAV's mass, and $g \approx 9.8$ m/s^2 is the gravitational acceleration.
- *Drag (D):* This is the aerodynamic force in the direction of the airflow. At a zero wind speed, D operates towards the reversed way of the UAV's heading.
- *Lift (L):* This is the force element in the direction perpendicular to the drag and lifting the UAV up.
- *Thrust (F):* This is the force generated by the UAV's engine, to surmount the drag and push the UAV forward and upward.

Given the UAV flying at a subsonic speed V, the drag is mathematically described as [24, Eqs. (4.1), (4.2), (4.13) & (4.14)]

$$D = c_1 V^2 + \frac{c_2 \kappa^2}{V^2}, \tag{6}$$

where $\kappa = L/W$ is the load factor, and c_1 and c_2 are known coefficients relying on the air density, and the wing surface and span of the aircraft [9].

For straight-and-level flight (SLF) and banked level turn (BLT), the power models of the UAV are derived in [9, App. A]. In this paper, we establish the power consumption for the ascending (and descending) of the UAV. We assume that the UAV takes straight ascending or descending (SAD), where the acceleration is in the same direction as the velocity, with no banked turn in any direction. It would be interesting to study in future the scenario where the UAV ascends or descends spirally, i.e., with centrifugal accelerations (i.e., banked turns) on both the (x, y)-plane and the (y, z)-plane.

As shown in Fig. 2, the acceleration a and the velocity V of the UAV monitor align with the thrust force F. The forces on the UAV obey the following equations:

$$F - D - W\sin\theta = ma, \tag{7a}$$

$$L = W\cos\theta, \tag{7b}$$

$$\sin\theta = V_z/V, \tag{7c}$$

$$\cos\theta = \sqrt{V_x^2 + V_y^2}/V, \tag{7d}$$

where V_x, V_y, and V_z are the components of the velocity parallel to the x-, y-, and z-axes, respectively. We have $\kappa = \cos\theta$. The power required for SAD is given by

$$P = |F|V = \left| c_1 V^3 + \frac{c_2\kappa^2}{V} + WV_z + maV \right|. \tag{8}$$

In (7c), $\sin\theta$ is positive when the UAV ascends, and negative when the UAV descends. This is intuitive, as ascending consumes more energy than descending due to the gravity.

It is derived in [9, Eq. (30)] that the load factor of level flight (including SLF and BLT) is upper bounded and approximated by $\kappa = \sqrt{1 + a^2/g^2}$ (with $g \approx 9.8$ m/s^2 being the gravitational acceleration). Combining the values of κ for level flight and SAD, we develop an upper bound of the load factor for the 3D trajectory, which is given by $\kappa^2 = \cos^2\theta(1 + a^2/g^2)$. When $\cos\theta = 1$, κ^2 reduces to the case of level flight; when $\cos\theta < 1$, κ^2 serves as an upper bound for the SAD. To facilitate formulation and convexification of the optimization problem, we further relax the load factor κ^2 with its upper bound $\kappa^2 = \cos^2\theta(1 + a^2/g^2) \le \cos^2\theta + a^2/g^2$, which will be used in the ensuing derivations.

By substituting the upper bound of κ^2, the velocity $\boldsymbol{v}_t$ and acceleration $\boldsymbol{a}_t$ into (8), the propulsion power at time slot t is

$$\begin{aligned} P_v^t &= c_1\|\boldsymbol{v}_t\|^3 + \frac{c_2\kappa^2}{\|\boldsymbol{v}_t\|} + m(gv_{zt} + \boldsymbol{a}_t^T\boldsymbol{v}_t) \\ &\le c_1\|\boldsymbol{v}_t\|^3 + \frac{c_2(v_{xt}^2 + v_{yt}^2)}{\|\boldsymbol{v}_t\|^3} + \frac{c_2\|\boldsymbol{a}_t\|^2}{g^2\|\boldsymbol{v}_t\|} + m(gv_{zt} + \boldsymbol{a}_t^T\boldsymbol{v}_t). \end{aligned} \tag{9}$$

This provides the upper-bound propulsion power of the fixed-wing UAV under 3D movement.

The total energy consumption over time T is given by:

$$\begin{aligned} \sum_{t=1}^{N} P_v^t \le \sum_t c_1\|\boldsymbol{v}_t\|^3 + \frac{c_2(v_{xt}^2 + v_{yt}^2)}{\|\boldsymbol{v}_t\|^3} + \frac{c_2\|\boldsymbol{a}_t\|^2}{g^2\|\boldsymbol{v}_t\|} \\ + mg(z_T - z_0) + \frac{m}{2}(\|\boldsymbol{v}_T\|^2 - \|\boldsymbol{v}_0\|^2), \end{aligned} \tag{10}$$

where the initial elevation and speed of the UAV monitor z_0 and $\boldsymbol{v}_0$ are known in prior, and $m(\|\boldsymbol{v}_T\|^2 - \|\boldsymbol{v}_0\|^2)/2$ denotes the change of the UAV's kinetic energy [9].

IV. Proposed Algorithm for Disguised Tracking and Surveillance

A. Problem Statement

We intend to minimize the energy usage of the fixed-wing UAV monitor and maximize its disguise throughout a disguised video surveillance mission period. The problem of interest is formulated as

$$\min_{\{\boldsymbol{q}_t, \boldsymbol{v}_t, \boldsymbol{a}_t, \forall t = 1, \ldots, N\}} \sum_{t=1}^{N} (P_v^t - f_t)\delta \tag{11a}$$

$$\text{s.t.} \sum_{n=1}^{t} P_v^n \delta \le \sum_{n=1}^{t} P_s^n \delta + \eta_0 E_0, \forall t, \tag{11b}$$

$$d_{\min} \le d_t \le d_{\max}, \tag{11c}$$

$$z_l \le z_t,$$

$$(1), \tag{11d}$$

where (11b) ensures that the UAV monitor can have a minimum battery level of $(1 - \eta_0)E_0$ Joules at any slot in case of emergency.

Problem (11) is difficult to solve online due to the time-coupling in the 3D movement of the fixed-wing UAV, the non-convex power models P_v^t in (9), and the reliance on the correct prediction of the target trajectory. Traditional online algorithms are not effective in this case, as they would either result in a greedy optimization at the current slot or a coarse optimization over future slots with inaccurate predictions.

By exploiting receding horizon control (also known as model-predictive control) [13], we decouple the problem between time slots and solve the problem online slot-by-slot to progressively improve the trajectory on-the-fly. In particular, at any time slot τ, the monitoring UAV forecasts the target's flight path over the upcoming N slots. Applying the receding horizon control, the UAV monitor optimizes the 3D flight path of the monitor for the forthcoming N time slots (or steps). At slot $(\tau + 1)$, the monitor flies as planned for only a slot, and then forecasts the target's flight path again for the forthcoming N slots. The monitor adjusts its flight path according to its forecast of the target's trajectory. The forecast horizon of N slots keeps being shifted forward (by one slot at every step). The receding horizon control is known to provide excellent performance in real-world applications.

We assume that the UAV monitor keeps measuring and obtaining the positions and directions of the targeted UAV. At an arbitrary (present) slot, denoted by τ, the monitoring UAV forecasts the coordinates of the target for the next L slots ($L \le N$), i.e., $(\hat{b}_{x(\tau+t)}, \hat{b}_{y(\tau+t)}), t \le L$, according to the historical actions of the targeted object, e.g., by using Kalman filtering. The monitor's present coordinate is (x_τ, y_τ, z_τ). As shown in Fig. 3, the monitoring UAV designs its flight path for the next L time slots (from $\tau + 1$ up to $\tau + L$), by transforming problem (11)

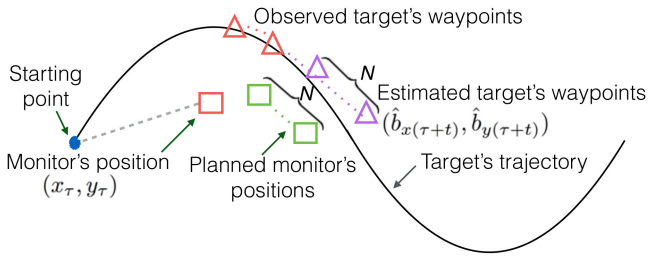

Fig. 3. A bird's view illustration of the online control approach.

into the following problem and solving at slot τ:

$$\min_{\{\boldsymbol{q}_t,\boldsymbol{v}_t,\boldsymbol{a}_t,\forall t=1,\ldots,N\}} \sum_{t=1}^{L}(P_v^{\tau+t} - f_{\tau+t}) \tag{12a}$$

$$\text{s.t.} \sum_{n=1}^{\tau+t} P_v^n \le \sum_{n=1}^{\tau+t} P_s^n(z_n) + \eta_0 E_0/\delta, \forall t, \tag{12b}$$

$$\boldsymbol{q}_{\tau+t+1} = \boldsymbol{q}_{\tau+t} + \boldsymbol{v}_{\tau+t}\delta + \frac{1}{2}\boldsymbol{a}_{\tau+t}\delta^2, \forall t, \tag{12c}$$

$$\boldsymbol{v}_{\tau+t+1} = \boldsymbol{v}_{\tau+t} + \boldsymbol{a}_{\tau+t}\delta, \forall t, \tag{12d}$$

$$\|\boldsymbol{a}_{\tau+t}\| \le a_{\max}, \|\boldsymbol{v}_{\tau+t}\| \le v_{\max}, \forall t, \tag{12e}$$

$$\|\boldsymbol{q}_{\tau+t} - \hat{\boldsymbol{b}}_{\tau+t}\| \le d_{\max}, z_l \le z_t, \forall t, \tag{12f}$$

$$\max\{v_{\min}, v_{z(\tau+t)}/\vartheta\} \le \|\boldsymbol{v}_{\tau+t}\|, \forall t, \tag{12g}$$

$$d_{\min} \le \|\boldsymbol{q}_{\tau+t} - \hat{\boldsymbol{b}}_{\tau+t}\|, \forall t. \tag{12h}$$

The non-convexity of the UAV mobility, propulsion power, harvested solar power, and visual disguise makes problem (12) hard to address by off-the-shelf convex solvers, e.g., the interior point method. The 3D movement of the fixed-wing UAV has to be jointly optimized, since its horizontal and vertical propulsion powers are closely coupled in (10). Moreover, the online planning of the monitor's trajectory at different positions and time slots are correlated and inter-dependent. All this makes it intangible to control the 3D trajectory and minimize the power usage of the fixed-wing UAV monitor. In the next section, we convexify the problem and solve it efficiently.

B. SCA-Based Per-Slot Trajectory Planning

We employ the successive convex approximation (SCA) [25] to deal with the non-convexity of problem (12) in pursuit of a computationally efficient solution for (12). The SCA progressively draws closer to the aforementioned upper limit of the propulsion power P_v^t, and replaces the concave component of (12a), i.e., $-f_t$, with a linear approximation to be readily tackled with convex programming.

By introducing slack variables $\zeta_t \le \|\boldsymbol{v}_t\|$ and $\xi_t \le \|\boldsymbol{v}_t\|^3, \forall t$, we can write the upper bound of P_v^t in (9) as

$$\hat{P}_v^t = c_1\|\boldsymbol{v}_t\|^3 + \frac{c_2(v_{xt}^2 + v_{yt}^2)}{\xi_t} + \frac{c_2\|\boldsymbol{a}_t\|^2}{g^2\zeta_t} + m\left(gv_{zt} + \boldsymbol{a}_t^T\boldsymbol{v}_t\right). \tag{13}$$

Problem (12) is transformed to:

$$\min_{\{\boldsymbol{q}_t,\boldsymbol{v}_t,\boldsymbol{a}_t,\zeta_t,\xi_t,\forall t=1,\ldots,L\}} \sum_{t=1}^{L}(\hat{P}_v^{\tau+t} - f_{\tau+t}) \tag{14a}$$

$$\text{s.t.} \sum_{n=1}^{\tau+t} \hat{P}_v^n\delta \le \sum_{n=1}^{\tau+t} P_s^n\delta + \eta_0 E_0, \forall t, \tag{14b}$$

$$\zeta_{\tau+t} \le \|\boldsymbol{v}_{\tau+t}\|, \forall t, \tag{14c}$$

$$\xi_{\tau+t} \le \|\boldsymbol{v}_{\tau+t}\|^3, \forall t, \tag{14d}$$

$$\zeta_{\tau+t} \ge v_{\min}, \xi_{\tau+t} \ge v_{\min}^3, \forall t,$$
$$(12b) - (12h). \tag{14e}$$

Despite the inequality constraints (14c) and (14d), the equivalence remains valid between problems (12) and (14). This is because, if (14c) and (14d) hold with tight inequality for an arbitrary t, we can always increase the values of ζ_t and ξ_t to suppress the energy consumption until (14c) and (14d) are satisfied with the equality [26].

Constraints (12g), (12h), (14c) and (14d) are non-convex. Nevertheless, the right-hand sides (RHSs) of the constraints are convex and differentiable in $\boldsymbol{v}_t$ or $\boldsymbol{q}_t$. They can be approached successively by using the first-order Taylor expansion at the local point attained during the ℓ-th iteration, as given by

$$\|\boldsymbol{v}_t\| \ge \|\boldsymbol{v}_t^{(\ell)}\| + \frac{(\boldsymbol{v}_t^{(\ell)})^T}{\|\boldsymbol{v}_t^{(\ell)}\|}\left(\boldsymbol{v}_t - \boldsymbol{v}_t^{(\ell)}\right) := \Gamma_{1t}, \tag{15a}$$

$$\|\boldsymbol{v}_t\|^3 \ge \|\boldsymbol{v}_t^{(\ell)}\|^3 + 3\|\boldsymbol{v}_t^{(\ell)}\|\left(\boldsymbol{v}_t^{(\ell)}\right)^T\left(\boldsymbol{v}_t - \boldsymbol{v}_t^{(\ell)}\right) := \Gamma_{2t}, \tag{15b}$$

$$d_t \ge \|\boldsymbol{q}_t^{(\ell)} - \boldsymbol{b}_t\| + \frac{(\boldsymbol{q}_t^{(\ell)})^T}{\|\boldsymbol{q}_t^{(\ell)} - \boldsymbol{b}_t\|}\left(\boldsymbol{q}_t - \boldsymbol{q}_t^{(\ell)}\right) := \hat{d}_t, \tag{15c}$$

where $(\cdot)^T$ stands for transpose. The non-convex constraints (12g), (12h), (14c) and (14d) are now convexified by:

$$\max\{v_{\min}, v_{z(\tau+t)}/\vartheta, \zeta_{\tau+t}\} \le \Gamma_{1(\tau+t)}, \forall t, \tag{16a}$$

$$\xi_{\tau+t} \le \Gamma_{2(\tau+t)}, \forall t, \tag{16b}$$

$$d_{\min} \le \hat{d}_{\tau+t}, \forall t. \tag{16c}$$

We offer a lower limit for the concave solar power $P_s^t(z_t)$ through approximating the concave function by a linear expression, as given by

$$\hat{P}_s^t(z_t) := c_3 z_t + c_4, \tag{17}$$

where c_3 and c_4 are known scaling weights relying on the efficiency and amount of solar energy harvesting. Constraint (14b) and, in turn, (12b), can be convexified and tightened by:

$$\sum_{n=1}^{\tau+t} \hat{P}_v^n\delta \le \sum_{n=1}^{\tau+t} \hat{P}_s^n\delta + \eta_0 E_0, \forall t. \tag{18}$$

We do not perform the first-order Taylor expansion of the concave solar power $P_s^t(z_t)$, as it provides an upper bound

for $P_s^t(z_t)$, not a lower bound. In the considered system, the approximation (17) offers a tight lower limit for $P_s^t(z_t)$ [22].

We proceed to convexify the concave part in the objective of (12), i.e., $-f_t$. Since f_t is convex, its global lower bound can be successively approached by plugging the first-order Taylor expansion at the local point attained during the ℓ-th iteration:

$$\begin{aligned} f_t \geq\ & f_t(\boldsymbol{q}_t^{(\ell)}) + 2\mu_1 \left(x_t^{(\ell)} - b_{xt}\right)\left(x_t - x_t^{(\ell)}\right) \\ & + 2\mu_1 \left(y_t^{(\ell)} - b_{yt}\right)\left(y_t - y_t^{(\ell)}\right) \\ & + 2\mu_2 \left(z_t^{(\ell)} - z_{t-1}^{(\ell)}\right)\left[(z_t - z_t^{(\ell)}) - (z_{t-1} - z_{t-1}^{(\ell)})\right] \\ & := \hat{f}_t, \end{aligned}$$

where $\hat{f}_t$ is a linear function of $\boldsymbol{q}_t$.

Let $P_v = \sum_{t=1}^{L} \hat{P}_v^{\tau+t}$ and $f = \sum_{t=1}^{L} \hat{f}_{\tau+t}$. Since P_v is a convex function and $\hat{f}_t$ (therefore, f) is a linear function, their difference is a convex function. Problem (14) can be transformed into the following convex program:

$$\begin{aligned} & \min_{\{\boldsymbol{q}_t, \boldsymbol{v}_t, \boldsymbol{a}_t, \zeta_t, \xi_t, \forall t=1,\ldots,L\}} P_v - f \\ & \text{s.t.} (12c) - (12f), (14e), (16), \text{and} (18). \end{aligned} \tag{19}$$

The objective function and the constraints of (19) are all convex. Problem (19) can be readily tackled by standard convex solvers, e.g., the interior point method.

Given the global upper limit of P_v^t in (13) and the lower bounds in (15) and (17), constraints (16) and (18) tighten the original constraints (12g), (12h) and (12b), respectively. When the constraints of (19) are fully obeyed, the constraints of the initial problem (12) are fully obeyed; not the other way around. Hence, the feasible solution region of problem (19) is just part of that of problem (12). The minimum objective of (19) is an upper bound of the objective of (12). As proved in [26], the SCA-based approach can converge to at least a stationary point of problem (14). Therefore, integrating SCA into the MPC framework can generate a solution that is a stationary point at each optimization slot τ.

The proposed approach is summarized in Algorithm 1, which is computationally dominated by Step 9. Specifically, Steps 5 to 7 compute linear functions with a complexity of $\mathcal{O}(N)$. After a series of mathematical transformations, Step 9 tackles a convex program and refreshes the design variables by running the interior point method, whose complexity is $\mathcal{O}(N^{3.5})$ per round (or iteration). By summarizing every optimization procedure, the overall complexity of Algorithm 1 is $\mathcal{O}(N^{3.5})$ each round. Given the convergence precision ϵ, Algorithm 1 has a polynomial complexity of $\mathcal{O}(N^{3.5}\log\frac{1}{\epsilon})$, wherein $\mathcal{O}(\log\frac{1}{\epsilon})$ accounts for the number of rounds before convergence to a suboptimal solution to problem (12).

V. Numerical and Simulation Results

This section provides MATLAB simulation results to substantiate the commendable traits of our proposed scheme. Parameters regarding the UAV monitor's energy usage and reaped solar energy are provided in Table I. The overall mission duration is $T = 30$ seconds with a duration of 0.2 s per slot ($N = 150$). The minimum and maximum distances from the target to the monitor in the 3D space are $d_{\min} = 3$ m and $d_{\max} = 20$ m, respectively. The linear flight path of the target is simulated by $b_{xt} = 9t$ and $b_{yt} = 0$. At slot τ, the estimated target trajectory is generated by $(\hat{b}_{x(\tau+t)}, \hat{b}_{y(\tau+t)}) = (b_{x(\tau+t)}, b_{y(\tau+t)}) + \varepsilon_t, \forall t$, where ε_t is the estimation error following the zero-mean Gaussian distribution. The weighting coefficients of disguise are $(\mu_1, \mu_2) = (0.4, 0.6)$, unless otherwise stated. The initial trajectory of the monitor is set as $x_t = 8t$ and $y_t = 0$ for the first optimization slot $\tau = 1$. The optimized trajectory of the previous slot τ initializes the trajectory of the new slot $\tau + 1$.

TABLE I
Simulation Parameters for the Fixed-Wing UAV monitor [9], [27]

Parameter	Value
The weight of the fixed-wing UAV	4 kg
Coefficients for the fixed-wing UAV, c_1 and c_2	9.26×10^{-4}, 2050
Lower and upper bounds of the speed, $v_{\min}$ and $v_{\max}$	4 m/s, 30 m/s
Maximum acceleration, $a_{\max}$	4 m/s^2
Sine of the maximum pitch angle, ϑ	0.7
Gaseous obliteration, α	0.8978
Radiation intensity of solar waves, P_i	1367 W/m^2
Efficiency and size of solar panel, η and S	0.4, 0.5 m^2
Initial battery level, E_0	4000 J
Fraction of consumable energy in the battery, η_0	0.5
Starting elevation of the target and monitor, H and z_0	100 m, 102 m
Constants for energy harvesting approximation, c_3 and c_4	0.0097, 165.83

Algorithm 1: The Receding Horizon Control-Based Online Approach for Problem (12).

1: At an arbitrary time slot τ, the UAV monitor measures and obtains the present position of the target and forecasts its waypoints in the ensuing L slots.
2: Attain the lower bound on the harvested solar power $P_s^t(z_t)$ by a linear approximation in (17).
3: **Initialization:** Generate a feasible initial flight path for the monitor, i.e., $\{\boldsymbol{q}_t^{(0)}, \boldsymbol{v}_t^{(0)}, \boldsymbol{a}_t^{(0)}, t = 1, \ldots, L\}$, and input initial values for the slack variables $\{\zeta_t^{(0)}, \xi_t^{(0)}, t = 1, \ldots, L\}$.
4: **for** $\ell = 0, 1, 2, \ldots$ **do**
5: Approximate the propulsion power P_v^t by (13), (15), and (16) by the SCA technique.
6: Convexify constraints (12g), (12h), (14c) and (14d) by (15) and (16).
7: Linearize the concave part in the objective of (12), i.e., $-f_t$, with the SCA technique.
8: Transform problem (12) to problem (19).
9: Solve problem (19) with the interior point method and update the optimization variables $\{\boldsymbol{q}_t^{(\ell)}, \boldsymbol{v}_t^{(\ell)}, \boldsymbol{a}_t^{(\ell)}\}$ to design the UAV monitor's flight path for the forthcoming L slots.
10: Implement the first step of the L waypoints.
11: Update $\ell \leftarrow \ell + 1$.
12: **end for**

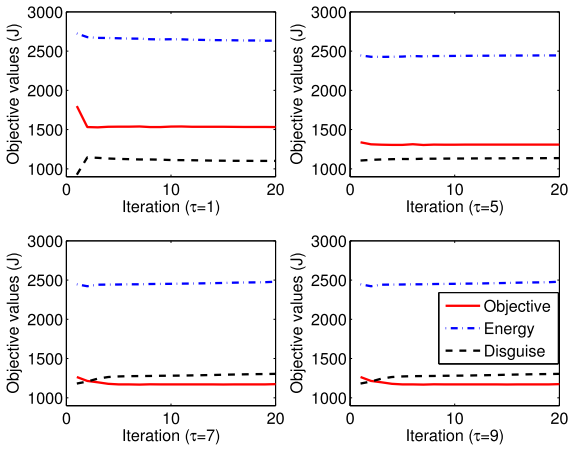

Fig. 4. Convergence of the proposed online scheme at different optimization slot τ with $L = 50$.

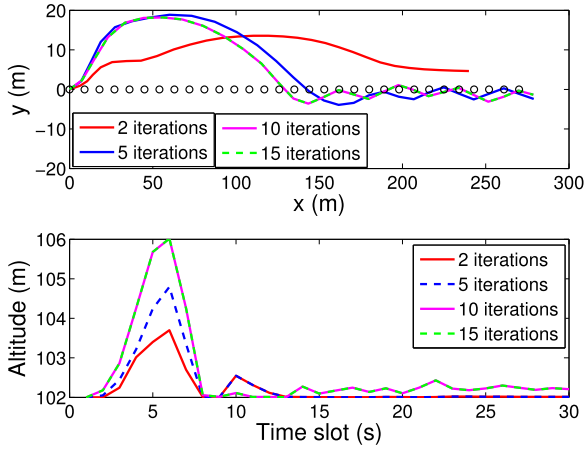

Fig. 5. 3D trajectory of the monitor by the proposed online scheme with different numbers of iteration when $L = 50$.

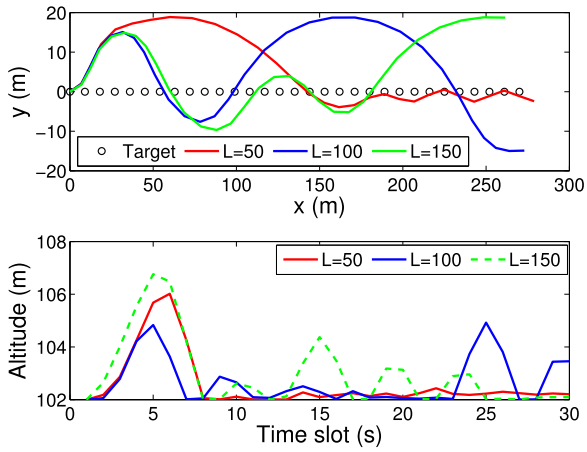

Fig. 6. 3D trajectory of the UAV monitor by different online schemes.

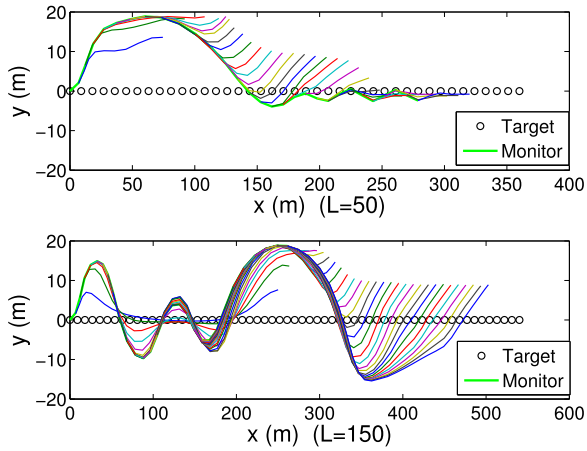

Fig. 7. Horizontal trajectory of the UAV monitor at each optimization slot τ by the online scheme, where the black circle is the target trajectory, the green line is the optimized monitor trajectory, and the other trajectories in different colors are the planned L-step trajectories at each slot.

We show the performance of the proposed MPC-based online approach. At each optimization slot τ, L steps of the trajectory are planned for the monitor by running Algorithm 1 until convergence. Fig. 4 depicts the convergence of the online algorithm when $L = 50$. The red solid curve depicts the objective value of problem (12). The blue dash-dot curve depicts the sum energy usage of the monitoring UAV $P_v\delta$; see (19). The black dashed (non-decreasing) curve depicts the disguise measure f. It can be seen that the objective values (in Joules) converge fast within 10 iterations per slot τ, and become stable within 5 optimization slots. Fig. 5 depicts the monitor trajectory by running the online approach for different numbers of iteration per slot τ when $L = 50$. It is revealed that the trajectory planning can achieve a desirable performance within 15 iterations per slot.

Fig. 6 plots the 3D trajectory of the fixed-wing UAV monitor by the proposed online scheme with different numbers of planned waypoints L. It is observed that the trajectory is improved with the increasing numbers of the planned waypoints per slot. Horizontally, the UAV follows and monitors the target with a reasonable spatial remoteness. Vertically, the monitor varies its elevation continuously, frequently deviating from the moving direction of the target. Fig. 7 depicts the planned trajectory of the monitor at each optimization slot τ for $L = 50$ and $L = 150$, respectively. It is seen that the trajectory is progressively refined over time by implementing one step at each slot. The objective values of the corresponding schemes are provided in Fig. 8. By comparing the performances of $L = 50$ and $L = 150$, we see that the energy consumption is significantly reduced and the visual disguise is enhanced as a result of the trajectory planning over a longer period.

Fig. 9 illustrates the distance from the target to the monitor on the (x, y)-plane, and the movement of the monitoring UAV in the view of the target by the online scheme with $L = 100$. The target is viewed as an anchor mark and highlighted by a green diamond. The relative waypoints are $(x_t - b_{xt}, y_t - b_{yt}), \forall t$. The target is located at (0,0) in the figure. It is revealed in Fig. 9 that the UAV monitor travels first northwestern then southeastern to the target, at a reasonable 3D remoteness within the range of $[d_{\min}, d_{\max}] = [3, 20]$ meters. In the view of the target, the UAV monitor demonstrates stochastic traveling patterns.

Fig. 10 shows the battery level (in Wh) of the UAV monitor at each time slot during the surveillance mission, with and without solar energy reaping. It is observed that the sustainability of

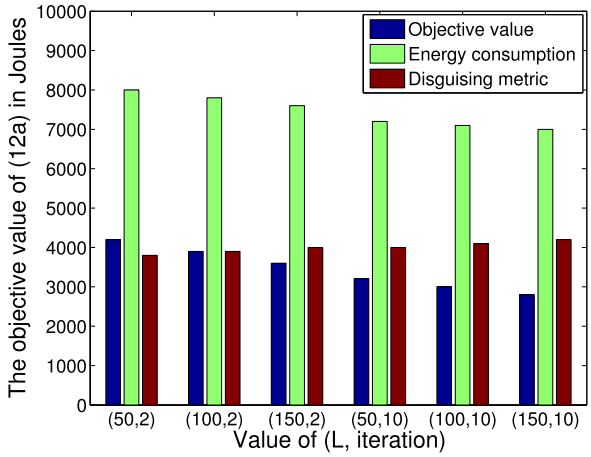

Fig. 8. Objective values of the UAV monitor by different online schemes over $T = 30$ seconds.

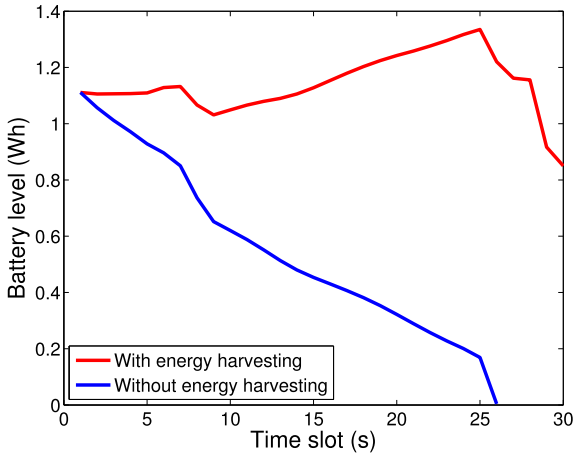

Fig. 10. Battery level of the monitor with and without solar energy harvesting.

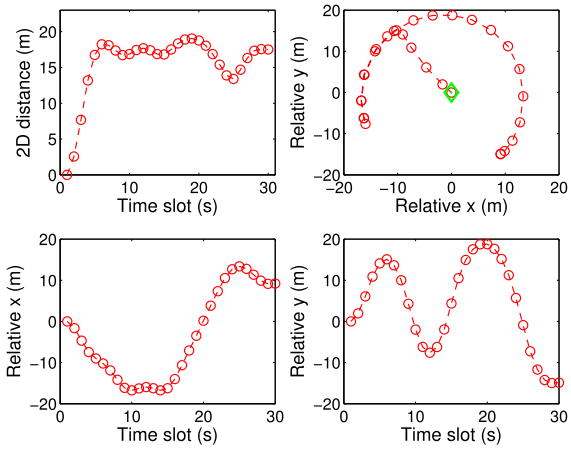

Fig. 9. Relative 2D monitor trajectory in the view of the target by the online scheme with $L = 100$.

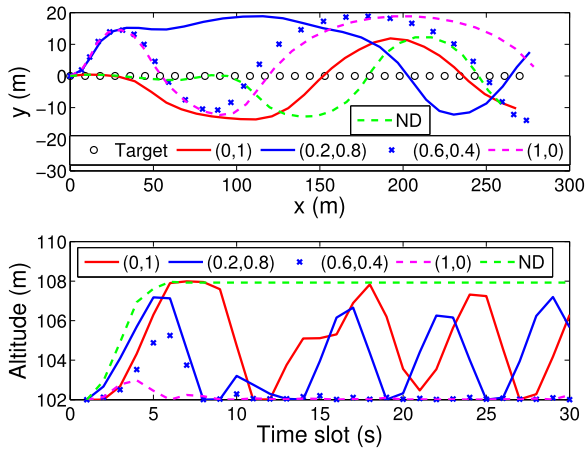

Fig. 11. 3D trajectory of the UAV monitor by different online schemes with $L = 100$.

the monitor can be enhanced with solar energy reaping, and the residual energy in the battery is always above $(1 - \eta_0)E_0$ at any time slot for emergency. While the battery capacity can only support the UAV flight for 26 seconds without energy harvesting. The merits of solar energy harvesting is therefore corroborated.

By varying the weighting coefficients of disguise (μ_1, μ_2), we show their influence on the objective value and the flight path of the monitoring UAV optimized online with the proposed Algorithm 1. Fig. 11 depicts the 3D trajectory of the UAV monitor by Algorithm 1 and the baseline schemes (i.e., partial or no disguise) with $L = 100$. The baseline scheme without visual disguise is labeled as "No Disguise" or "ND" for short. It is shown that, compared to the ND scheme, the proposed algorithm strikes a good balance between distance keeping and elevation varying, and results in effective visual disguise. It is also shown in Fig. 11 that the visual disguise is more susceptible to the elevation of the UAV monitor than the horizontal target-monitor spatial separation. When the weighting coefficient of the elevation variance is lifted from 0 to 1, the elevation varies increasingly frequently. Fig. 12 presents the corresponding objective values of problem (12) in each scenario. By comparing between $(\mu_1, \mu_2) = (0, 1)$ and $(1, 0)$, we can draw the conclusion that maintaining the horizontal target-monitor separation is more effective to suppress the objective value than varying the height of the monitor. On the other hand, raising the weighting coefficients of disguise cannot improve the efficiency boundlessly, as the monitor is increasingly restrained by its maximum velocity and the 3D distance from the target. The energy consumption of the ND scheme is the lowest, as the monitor flies in the most energy-efficient way.

Fig. 13 depicts the performance of the online algorithm when the monitor's estimation on the target trajectory gets increasingly inaccurate over time, i.e., the estimation error increases with time and is generated by $0.5t\varepsilon_t$, when $(\mu_1, \mu_2) = (0.4, 0.6)$. It is unveiled that as the estimation error rises, the monitor takes less horizontal twist and turns, keeps a fair 2D distance from the target, travels in a relatively stable direction to the target on the (x, y)-plane, and changes its elevation more frequently, especially when $L = 150$. This is because the fixed-wing UAV changes its velocity continuously with no sudden or sharp movements due to its maneuverability and aerodynamics. Therefore, it seeks visual disguise in the direction that is more stable with less randomness to have robustness against the estimation error.

We proceed to show the performance of the fixed-wing UAV monitor under the offline scheme, by running Algorithm 1

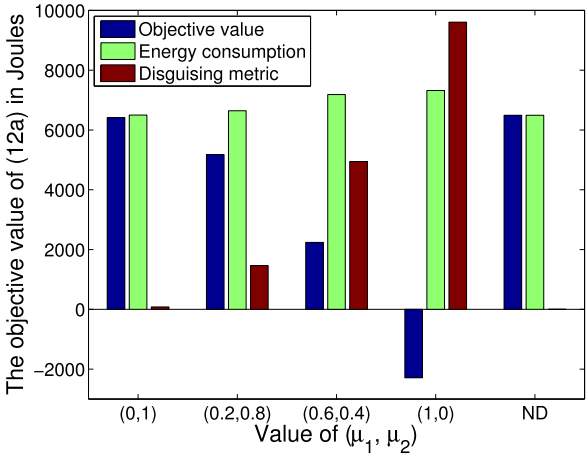

Fig. 12. Objective values of the UAV monitor by different online schemes with $L = 100$.

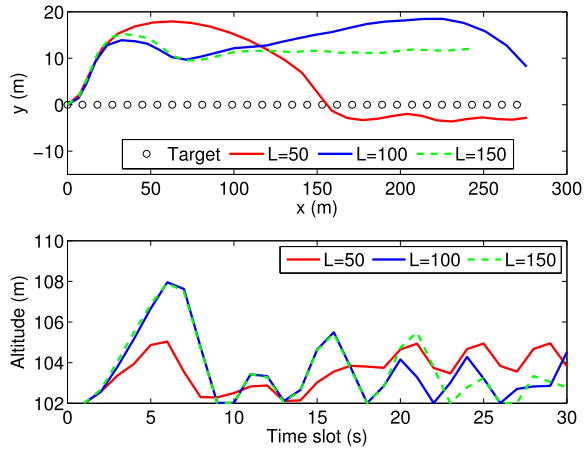

Fig. 13. 3D trajectory of the UAV monitor by the online scheme with an increasing estimation error over time when $(\mu_1, \mu_2) = (0.4, 0.6)$.

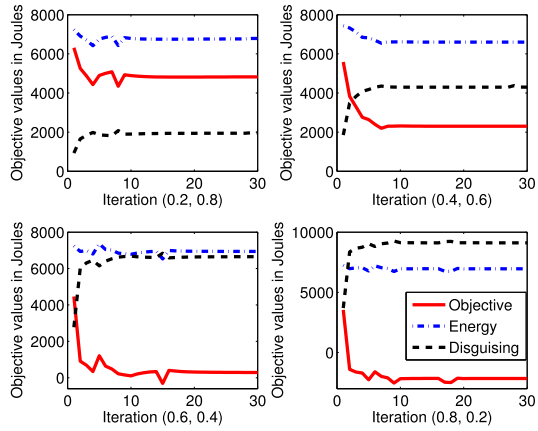

Fig. 14. Convergence of the objective values in (11a) by the offline scheme with different (μ_1, μ_2).

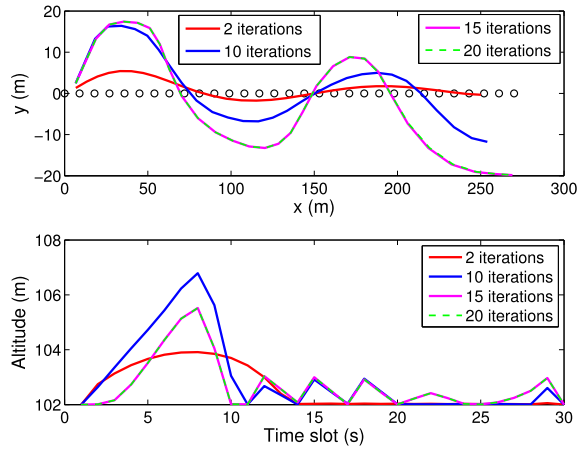

Fig. 15. Convergence of the 3D monitor trajectory by the offline scheme with $(\mu_1, \mu_2) = (0.4, 0.6)$.

to solve problem (11) with perfect *a-priori* knowledge of the target's trajectory over the scheduling period of $T = 30$ seconds. Fig. 14 depicts the convergence rate of the offline scheme with different values of (μ_1, μ_2). Fig. 14 unveils that the objective of (11) becomes stable and converges quickly in less than 30 iterations. The objective values converge faster when $\mu_1 < \mu_2$. The 3D trajectory of the fixed-wing UAV monitor with $(\mu_1, \mu_2) = (0.4, 0.6)$ is delineated in Fig. 15, where both the horizontal trajectory and the elevation variance become stable and converge in less than 20 iterations.

The 3D trajectories of the offline scheme and the baseline scheme are depicted in Fig. 16. The corresponding objective values are provided in Fig. 17. By comparing these two figures with Figs. 11 and 12, it is revealed that the online algorithm is as effective as the offline algorithm, but yielding a slightly higher energy consumption and lower disguising performance, due to the estimation error of the target trajectory. By optimizing $L = 100$ waypoints per slot τ, the online algorithm can achieve a desirable performance as compared to the offline scheme.

We compare the performances of disguised video surveillance between the fixed-wing UAV and its rotary-wing counterpart adjusting its trajectory online based on the receding horizon control model. For the convenience of readers, we provide the propulsion power model and the thrust power model of the rotary-wing UAV. The propulsion power for level flight is given by [22]

$$P_{lf}^t = P_0\left(1 + \frac{3V_h^{t2}}{U_{tip}^2}\right) + P_1\left(\sqrt{1 + \frac{V_h^{t4}}{4v_0^4}} - \frac{V_h^{t2}}{2v_0^2}\right)^{\frac{1}{2}} + \frac{1}{2}d_f \rho s A V_h^{t3}, \tag{20}$$

where V_h^t is the horizontal speed of the rotary-wing UAV at time slot t, given by $V_h^t = \sqrt{(x_t - x_{t-1})^2 + (y_t - y_{t-1})^2}/\delta$. The thrust power for vertical flight can be obtained by [22]

$$P_{vf}^t = W(z_t - z_{t-1})/\delta, \forall t. \tag{21}$$

Therefore, the power usage of the rotary-wing UAV at time slot t is $P_v^t = P_{lf}^t + P_{vf}^t$. The notations and values of the simulated parameters are provided in Table II.

We plot the 3D trajectory of the rotary-wing monitor in Fig. 18 by running the online Algorithm 1 with $L = 100$, and $(\mu_1, \mu_2) = (0.4, 0.6)$. It is observed that the rotary-wing monitor takes more and sharper horizontal turns, keeps a large horizontal

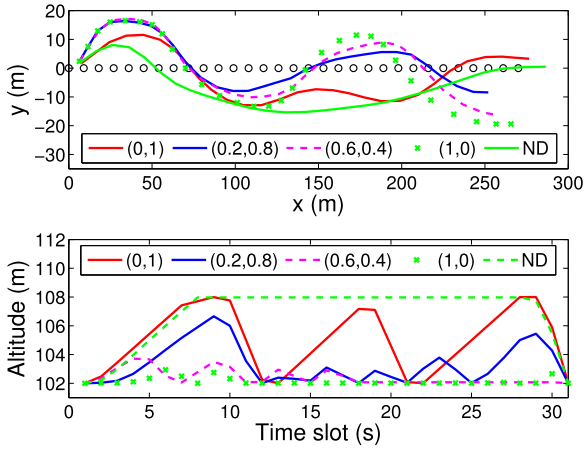

Fig. 16. 3D trajectory of the UAV monitor by the offline and baseline schemes.

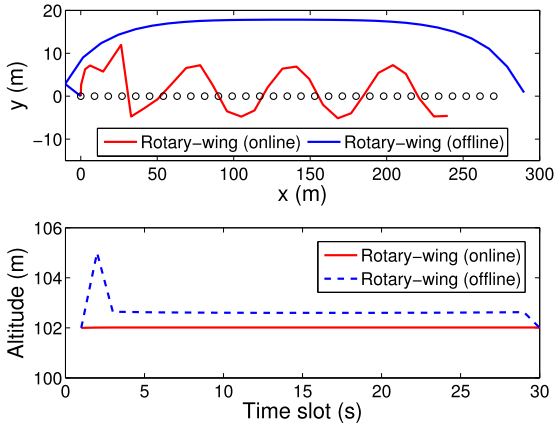

Fig. 18. 3D trajectory of the rotary-wing UAV monitor by the proposed schemes with $L = 100$ and $(\mu_1, \mu_2) = (0.4, 0.6)$.

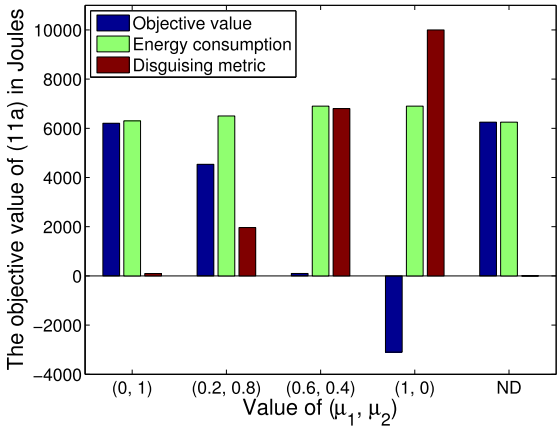

Fig. 17. Objective values of the UAV monitor by different offline schemes.

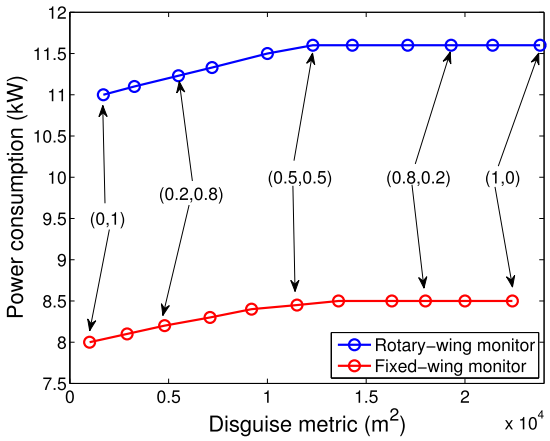

Fig. 19. Power consumption versus disguising metric under different values of (μ_1, μ_2) with $\mu_1 + \mu_2 = 1$ for fixed-wing and rotary-wing UAV monitors running the online trajectory planning algorithm when $T = 60$ seconds.

TABLE II
THE PARAMETERS OF THE ROTARY-WING UAV [26]

Parameter	Value
The weight of the rotary-wing UAV	4 kg
Blade profile power and tip speed, P_0 and U_{tip}	3.4 W, 60 m/s
Rotor induced power and velocity, P_1 and v_0	118 W, 5.4 m/s
Rotor solidity and disc area, s and A	0.05, 0.5 m^2
Air density and fuselage drag fraction, ρ and d_f	1.225 kg/m^3, 0.3

distance from (and behind) the target, shows more randomness and better visual disguise on the (x, y)-plane, and does not change its altitude, as compared to the fixed-wing monitor (as plotted in Fig. 16). While the rotary-wing monitor travels more smoothly by the offline scheme, flies first behind and then ahead of the target, and always appears on the same side of the target. Fig. 19 shows the Pareto-front between the energy usage and the disguise measure by changing the numerical quantities of μ_1 and μ_2 ($\mu_1 + \mu_2 = 1$). Fig. 19 shows that although the fixed-wing monitor scores a bit lower in disguise than the rotary-wing monitor, it is more energy-efficient and sustainable. The power consumption stops growing once the disguise measure surpasses 14,000 (m^2) for the fixed-wing monitor, and 12,000 (m^2) for the rotary-wing monitor.

We show the performance of the proposed online scheme for the fixed-wing and rotary-wing monitors under different target trajectories, i.e., a sinusoidal trajectory and a random trajectory. It can be observed from Figs. 20 and 21 that the monitors demonstrate good visual disguise under different target trajectories.

Finally, we show the performance of the proposed online scheme under a linear target trajectory when the mission duration is $T = 90$ s, and the maximum and minimum monitor-target distances are $d_{\max} = 100$ m and $d_{\min} = 20$ m. The reason is that the typical resolution of the cameras mounted on UAVs can recognize an object at a relatively large distance, e.g., over 100 m, when the cameras are reasonably concentrated. Fig. 22 plots the 3D trajectory of the fixed-wing UAV, and the battery level of the UAV with and without energy harvesting (labeled as "W/EH" and "W/O EH," respectively). We see that the UAV monitor can effectively follow the target, while keeping a reasonable distance of no larger than 100 m from the target. Moreover, the UAV can always maintain an energy reserve of no less than $(1 - \eta_0)E_0$ Joules in its battery with solar energy harvesting. In contrast, without energy harvesting, the battery energy can only support the UAV for 40 seconds of the mission.

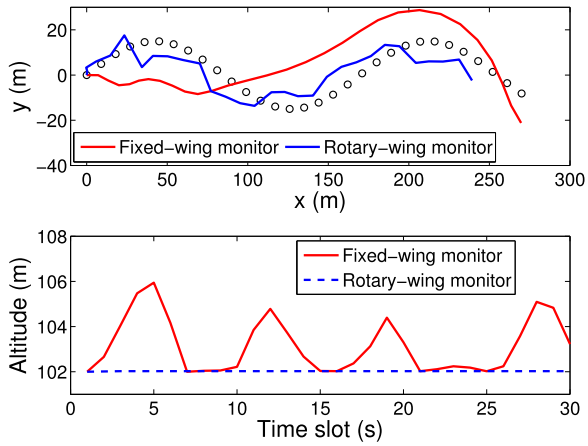

Fig. 20. 3D trajectory of the fixed-wing and rotary-wing monitors by the proposed online scheme under a sinusoidal target trajectory with $L = 100$ and $(\mu_1, \mu_2) = (0.4, 0.6)$.

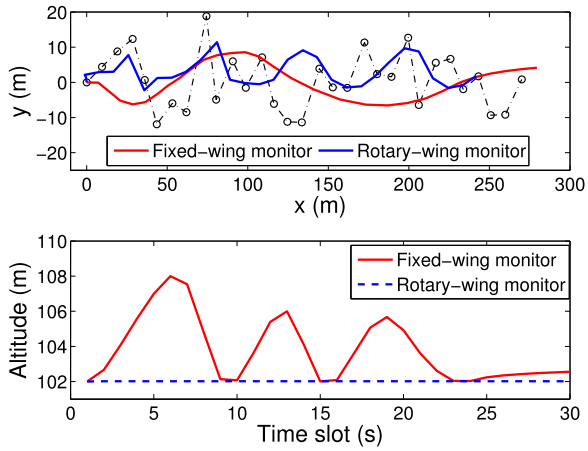

Fig. 21. 3D trajectory of the fixed-wing and rotary-wing monitors by the proposed online scheme under a random target trajectory with $L = 100$ and $(\mu_1, \mu_2) = (0.4, 0.6)$.

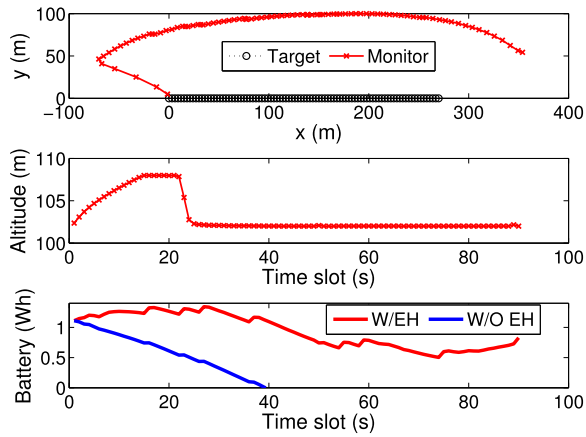

Fig. 22. 3D trajectory and battery level of the fixed-wing UAV monitor by the proposed online scheme under a linear target trajectory with $T = 90$ s, $d_{\max} = 100$ m, $L = 100$, and $(\mu_1, \mu_2) = (0.4, 0.6)$.

VI. Concluding Remark

In this paper, a new scheme was developed to exploit the maneuverability of a solar-powered, fixed-wing UAV for disguised tailing and video surveillance collectively through energy management and trajectory optimization. The SCA technique was employed to convexify the investigated problem, and integrated with the MPC framework in pursuit of a computationally efficient, quality solution in an online fashion. As corroborated by extensive simulations, the proposed scheme outperformed the schemes with no or partial disguise, in terms of visual disguise. The fixed-wing UAV was also demonstrated to surpass its rotary-wing counterpart with regard to energy efficiency and sustainability.

References

[1] E. T. Alotaibi, S. S. Alqefari, and A. Koubaa, "LSAR: Multi-UAV collaboration for search and rescue missions," *IEEE Access*, vol. 7, pp. 55817–55832, 2019.

[2] C. Yuan, Z. Liu, and Y. Zhang, "Learning-based smoke detection for unmanned aerial vehicles applied to forest fire surveillance," *J. Intell. Robot. Syst.*, vol. 93, no. 1, pp. 337–349, Feb. 2019.

[3] K. Li, W. Ni, X. Wang, R. Liu, S. Kanhere, and S. Jha, "Energy-efficient cooperative relaying for unmanned aerial vehicles," *IEEE Trans. Mobile Comput.*, vol. 15, no. 6, pp. 1377–1386, Jun. 2016.

[4] C. Sun, W. Ni, and X. Wang, "Joint computation offloading and trajectory planning for UAV-assisted edge computing," *IEEE Trans. Wireless Commun.*, vol. 20, no. 8, pp. 5343–5358, Mar. 2021.

[5] X. Yuan, Z. Feng, W. Ni, R. P. Liu, J. A. Zhang, and W. Xu, "Secrecy performance of terrestrial radio links under collaborative aerial eavesdropping," *IEEE Trans. Inf. Forensics Secur.*, vol. 15, pp. 604–619, 2020.

[6] S. Hu, Q. Wu, and X. Wang, "Energy management and trajectory optimization for UAV-enabled legitimate monitoring systems," *IEEE Trans. Wireless Commun.*, vol. 20, no. 1, pp. 142–155, Jan. 2021.

[7] H. Huang and A. Savkin, "An algorithm of reactive collision free 3-D deployment of networked unmanned aerial vehicles for surveillance and monitoring," *IEEE Trans. Ind. Informat.*, vol. 16, no. 1, pp. 132–140, Jan. 2020.

[8] S. Karim, Y. Zhang, A. A. Laghari, and M. R. Asif, "Image processing based proposed drone for detecting and controlling street crimes," in *Proc. 17th IEEE Int. Conf. Commun. Technol.*, 2017, pp. 1725–1730.

[9] Y. Zeng and R. Zhang, "Energy-efficient UAV communication with trajectory optimization," *IEEE Trans. Wireless Commun.*, vol. 16, no. 6, pp. 3747–3760, Jun. 2017.

[10] X. Zhang, Y. Fang, X. Zhang, J. Jiang, and X. Chen, "A novel geometric hierarchical approach for dynamic visual servoing of quadrotors," *IEEE Trans. Ind. Electron.*, vol. 67, no. 5, pp. 3840–3849, May 2020.

[11] H. Huang, A. Savkin, and W. Ni, "A method for covert video surveillance of a car or a pedestrian by an autonomous aerial drone via trajectory planning," in *Proc. IEEE Int. Coalition Inclusive Sustain. Cities*, 2020, pp. 1–3.

[12] H. Huang and A. Savkin, "Reactive 3D deployment of a flying robotic network for surveillance of mobile targets," *Comput. Netw.*, vol. 161, pp. 172–182, Oct. 2019.

[13] Y. Huang, H. Wang, and P. Yao, "Energy-optimal path planning for solar-powered UAV with tracking moving ground target," *Aerosp. Sci. Tech.*, vol. 53, pp. 241–251, Jun. 2016.

[14] L. Zhang *et al.*, "Vision-based target three-dimensional geolocation using unmanned aerial vehicles," *IEEE Trans. Ind. Electron.*, vol. 65, no. 10, pp. 8052–8061, Oct. 2018.

[15] P. Yao, Z. Xie, and P. Ren, "Optimal UAV route planning for coverage search of stationary target in river," *IEEE Trans. Control Syst. Tech.*, vol. 27, no. 2, pp. 822–829, Mar. 2019.

[16] V. Shaferman and T. Shima, "Unmanned aerial vehicles cooperative tracking of moving ground target in urban environments," *J. Guid. Control Dyn.*, vol. 31, no. 5, pp. 1360–1371, 2008.

[17] H. Yu, K. Meier, M. Argyle, and R. W. Beard, "Cooperative path planning for target tracking in urban environments using unmanned air and ground vehicles," *IEEE/ASME Trans. Mechatronics*, vol. 20, no. 2, pp. 541–552, Apr. 2015.

[18] S. A. Quintero and J. P. Hespanha, "Vision-based target tracking with a small UAV: Optimization-based control strategies," *Control Engineer. Pract.*, vol. 32, pp. 28–42, 2014.
[19] S. Schopferer, M. Brizon, C. Liersch, and S. Froese, "Evaluating the energy balance of high altitude platforms at early design stages," in *Proc. Int. Conf. Unmanned Aircr. Syst.*, 2016, 170–177.
[20] *SolarXOne: Autonomous UAV Technology*, Dec. 2021. https://xsun.fr/autonomous-drone/
[21] *SB4 Phoenix: Professional Long Range Drone*, Dec. 2021, https://sunbirds.aero/sb4-phoenix-long-range
[22] S. Hu, W. Ni, X. Wang, A. Jamalipour, and D. Ta, "Joint optimization of trajectory, propulsion, and thrust powers for covert UAV-on-UAV video tracking and surveillance," *IEEE Trans. Inf. Forensics Secur.*, vol. 16, pp. 1959–1972, Jan. 2021.
[23] G. S. Aglietti, S. Redi, A. R. Tatnall, and T. Markvart, "Harnessing high-altitude solar power," *IEEE Trans. Energy Conver.*, vol. 24, no. 2, pp. 442–451, Jun. 2009.
[24] A. Filippone, *Flight Performance of Fixed and Rotary Wing Aircraft*. Washington, DC, USA: AIAA, 2006.
[25] Y. Yang, M. Pesavento, S. Chatzinotas, and B. Ottersten, "Successive convex approximation algorithms for sparse signal estimation with nonconvex regularizations," *IEEE J. Sel. Top. Signal Process.*, vol. 12, no. 6, pp. 1286–1302, Dec. 2018.
[26] Y. Zeng, J. Xu, and R. Zhang, "Energy minimization for wireless communication with rotary-wing UAV," *IEEE Trans. Wireless Commun.*, vol. 18, no. 4, pp. 2329–2345, Apr. 2019.
[27] A. Kokhanovsky, "Optical properties of terrestrial clouds," *Earth- Sci. Rev.*, vol. 64, no. 3, pp. 189–241, Feb. 2004.

Shuyan Hu (Member, IEEE) received the B.Eng. degree in electrical engineering from Tongji University, Shanghai, China, in 2014, and the Ph.D. degree in electronic science and technology from Fudan University, Shanghai, China, in 2019. She is currently a Postdoctoral Research Fellow with the School of Information Science and Technology, Fudan University. She was selected by the Shanghai Postdoctoral Excellence Program in 2019. Her research interests include convex and nonconvex optimizations, green communications, and UAV-aided communications.

Wei Ni (Senior Member, IEEE) received the B.E. and Ph.D. degrees in electronic engineering from Fudan University, Shanghai, China, in 2000 and 2005, respectively. He is currently a Principal Research Scientist with CSIRO, Sydney, NSW, Australia, and an Adjunct Professor with the University of Technology Sydney, Sydney, NSW, Australia, and an Honorary Professor with Macquarie University, Sydney, NSW, Australia. He was a Postdoctoral Research Fellow with Shanghai Jiao Tong University, Shanghai, China, from 2005 to 2008, the Deputy Project Manager with Bell Labs, Alcatel/Alcatel-Lucent from 2005 to 2008, and a Senior Researcher with Devices R&D, Nokia from 2008 to 2009. He has authored five book chapters, more than 200 journal papers, more than 80 conference papers, 25 patents, and ten standard proposals accepted by IEEE. His research interests include machine learning, online learning, stochastic optimization, and also their applications to system efficiency and integrity.

Dr. Ni has been the Chair of IEEE Vehicular Technology Society (VTS) New South Wales (NSW) Chapter since 2020 and the Editor of IEEE TRANSACTIONS ON WIRELESS COMMUNICATIONS since 2018. He was first the Secretary and then the Vice-Chair of IEEE NSW VTS Chapter from 2015 to 2019, the Track Chair of VTC-Spring 2017, the Track Co-Chair of IEEE VTC-Spring 2016, the Publication Chair of BodyNet 2015, and the Student Travel Grant Chair of WPMC 2014.

Xin Wang (Senior Member, IEEE) received the B.Sc. and M.Sc. degrees in electrical engineering from Fudan University, Shanghai, China, in 1997 and 2000, respectively, and the Ph.D. degree in electrical engineering from Auburn University, Auburn, AL, USA, in 2004.

From September 2004 to August 2006, he was a Postdoctoral Research Associate with the Department of Electrical and Computer Engineering, University of Minnesota, Minneapolis, MN, USA. In August 2006, he joined the Department of Electrical Engineering, Florida Atlantic University, Boca Raton, FL, USA, as an Assistant Professor, then was promoted to a tenured Associate Professor in 2010. He is currently a Distinguished Professor and the Chair of the Department of Communication Science and Engineering, Fudan University. His research interests include stochastic network optimization, energy-efficient communications, cross-layer design, and signal processing for communications. He is a Senior Area Editor of IEEE TRANSACTIONS ON SIGNAL PROCESSING and Editor of IEEE TRANSACTIONS ON WIRELESS COMMUNICATIONS. He was an Associate Editor for IEEE TRANSACTIONS ON SIGNAL PROCESSING, the Editor of IEEE TRANSACTIONS ON VEHICULAR TECHNOLOGY, and an Associate Editor for IEEE SIGNAL PROCESSING LETTERS. He is a Member of the Signal Processing for Communications and Networking Technical Committee of IEEE Signal Processing Society, and a Distinguished Lecturer of the IEEE Vehicular Technology Society.

Abbas Jamalipour (Fellow, IEEE) received the Ph.D. degree in electrical engineering from Nagoya University, Nagoya, Japan, in 1996. He holds the positions of a Professor of ubiquitous mobile networking with the University of Sydney, Sydney, NSW, Australia, and since January 2022, he has been the Editor-in-Chief of the IEEE TRANSACTIONS ON VEHICULAR TECHNOLOGY. He has authored nine technical books, eleven book chapters, more than 550 technical papers, and five patents, all in the area of wireless communications and networking. Prof. Jamalipour was the recipient of the number of prestigious awards, such as the 2019 IEEE ComSoc Distinguished Technical Achievement Award in Green Communications, 2016 IEEE ComSoc Distinguished Technical Achievement Award in Communications Switching and Routing, 2010 IEEE ComSoc Harold Sobol Award, 2006 IEEE ComSoc Best Tutorial Paper Award, and also more than 15 best paper awards. During 2020–2021, he was the President of IEEE Vehicular Technology Society. Previously, he held the positions of the Executive Vice-President and Editor-in-Chief of VTS Mobile World and has been an Elected Member of the Board of Governors of IEEE Vehicular Technology Society since 2014. He was the Editor-in-Chief of IEEE WIRELESS COMMUNICATIONS, the Vice President-Conferences, and a Member of Board of Governors of IEEE Communications Society. He sits on the Editorial Board of IEEE ACCESS and several other journals and is a Member of Advisory Board of the IEEE INTERNET OF THINGS JOURNAL. He is the General Chair or Technical Program Chair of several prestigious conferences, including the IEEE ICC, GLOBECOM, WCNC, and PIMRC. He is a Fellow of the Institute of Electrical, Information, and Communication Engineers (IEICE) and Institution of Engineers Australia, an ACM Professional Member, and an IEEE Distinguished Speaker.